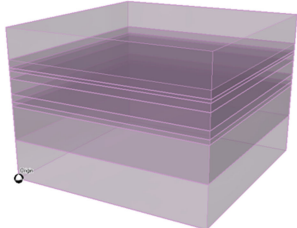
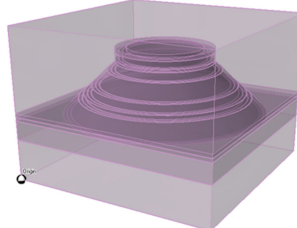
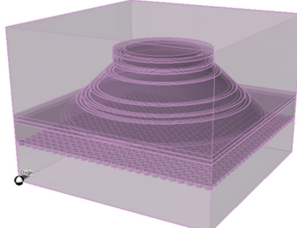
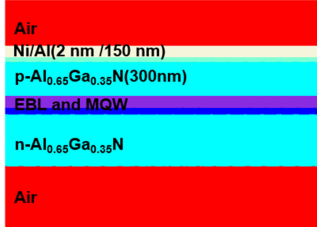
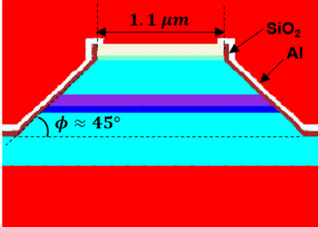
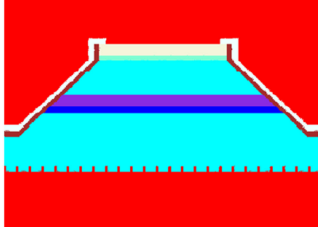


## Investigation of Light-Extraction Efficiency of Flip-Chip AlGaN-Based Deep-Ultraviolet Light-Emitting Diodes Adopting AlGaN Metasurface

Volume 13, Number 1, February 2021

Joosun Yun  
Hideki Hirayama

|                      | With flat n-AlGaN and infinite lateral size   | With flat n-AlGaN and Al/SiO <sub>2</sub> inclined sidewall   | With AlGaN metasurface and Al/SiO <sub>2</sub> inclined sidewall                      |
|----------------------|---|---|---|
| Transparent view     |    |    |  |
| Cross-sectional view |  <p>Air<br/>Ni/Al(2 nm /150 nm)<br/>p-Al<sub>0.65</sub>Ga<sub>0.35</sub>N(300nm)<br/>EBL and MQW<br/>n-Al<sub>0.65</sub>Ga<sub>0.35</sub>N<br/>Air</p> |  <p>1.1 μm<br/>SiO<sub>2</sub><br/>Al<br/><math>\phi \approx 45^\circ</math></p> |  |
| LEE                  | <p>TE = 7.33 %<br/>TM = 0.34 %</p>  | <p>TE = 56.3 %<br/>TM = 30.6 %</p>  | <p>TE = 57.8 %<br/>TM = 37.7 %</p>  |

DOI: 10.1109/JPHOT.2021.3054914

# Investigation of Light-Extraction Efficiency of Flip-Chip AlGaIn-Based Deep-Ultraviolet Light-Emitting Diodes Adopting AlGaIn Metasurface

Joosun Yun  and Hideki Hirayama

RIKEN, Wako 351-0198, Japan

DOI:10.1109/JPHOT.2021.3054914

This work is licensed under a Creative Commons Attribution 4.0 License. For more information, see <https://creativecommons.org/licenses/by/4.0/>

Manuscript received December 20, 2020; revised January 22, 2021; accepted January 24, 2021. Date of publication January 28, 2021; date of current version February 10, 2021. Corresponding author: Joosun Yun (e-mail: joosun.yun@riken.jp).

**Abstract:** Herein, we investigate the influence of an AlGaIn metasurface on AlGaIn-based deep-ultraviolet light-emitting diodes' light-extraction efficiency by utilizing the 3D finite-difference time-domain method. As the first step in this study, we optimize an AlGaIn metasurface to maximize the transmittance from LED to air. Then, six different flip-chip structures' light-extraction efficiencies are compared with each other to judge the usefulness of the metasurface's adoption on AlGaIn-based LED. Considered structures are classified into two categories, with and without inclined sidewall, respectively. Each classified structure is subdivided again by three factors: flat interface, roughed cones, and metasurface on n-AlGaIn. Extracted results show that the combination of inclined sidewall and the AlGaIn metasurface shows synergetic results positively increasing light-extraction efficiency.

**Index Terms:** Light-emitting diode, metasurface, finite-difference time-domain, deep ultraviolet.

## 1. Introduction

Deep-Ultraviolet light-emitting diodes (DUV-LEDs) in the wavelength  $\lambda \approx 220\text{--}350$  nm can cover broad and vital applications such as communication, photoionization, water purification, sterilization, medical diagnostics, UV curing, and plant lighting [1], [2]. However, for the successful domination of the represented application area, the attainment of high efficiency comparable to Mercury lamps is essential. The typical wall-plug-efficiency (WPE) of DUV-LEDs at the UVC range is below 6%, which is relatively lower than the WPE of Mercury lamps, 15-35% [3], [4]. The internal quantum efficiency (IQE) below 70% at room temperature, total internal reflection (TIR), severe light absorption by p-GaN and metallic layers, low conductivity of p-AlGaIn, efficiency droop phenomena, and continuously discovered new properties of  $\text{Al}_x\text{Ga}_{1-x}\text{N}$  quantum well (QW) are attributed to the origins for such low WPE of AlGaIn-based DUV-LEDs [5]–[10]. Among those factors to be solved, there have been many fruitful ideas about how to increase the light-extraction efficiency (LEE) of flip-chip DUV-LEDs. The adoption of Ni/Al metal electrode increasing reflectance, inclined sidewall structure tilting the light incident angles effectively, and p-AlGaIn transparent layer showing negligible DUV absorption are few examples of the successful ideas [11]–[13]. However, it is difficult to search for cases utilizing the dielectric metasurface for the LEE enhancement of flip-chip DUV-LEDs.

The dielectric metasurface in visible and infrared (IR) range has adopted materials of high refractive indexes ( $n$ ) such as Si, Ge, PbTe, AlGaAs, GaInP, and AlGaSb over  $n = 3.0$  with the low loss [14]. These materials are not appropriate for the application in the DUV range due to the high loss, so it is essential to find an appropriate material system having a low loss for the DUV light's manipulation. Additionally, since the high  $n$  implies the low escape cone angle toward the air, it will be advantageous to lower  $n$  as possible to increase the fundamental critical angle, from which TIR starts. The previous studies based on Mie theory predicted that with materials near  $n = 2.0$ , it is possible to observe similar plasmonic effects as the materials over  $n = 3.0$  [15]. Since the transparent hexagonal  $\text{Al}_x\text{Ga}_{1-x}\text{N}$  has  $n$  near and higher than 2.0 from  $x = 0$  to  $x = 0.65$  below the wavelength of about 827 nm, AlGaN can be a candidate material for DUV's low-loss dielectric metasurface [16].

Based on the backgrounds, we optimize a periodic  $n\text{-Al}_{0.65}\text{Ga}_{0.35}\text{N}$  metasurface, which can be adopted on flip-chip DUV-LEDs near wavelength  $\lambda = 280$  nm, by utilizing 3D finite-different time-domain (FDTD). The optimization is focused on increasing transmittance when light propagates from LED to air. The usefulness of the optimized metasurface as a light extractor is estimated by comparing LEEs among six different flip-chip structures. For the investigation of the AlGaN metasurface, we lift off AlN/Sapphire layers since the AlN or Sapphire is too challenging to trigger Mie-based resonance due to small  $n$  and short target wavelength. The contents of this study are as follows. Section 2 details the utilized modeling methods and techniques used for this study's entire calculation. The optimization process and analysis for AlGaN metasurface based on a unit cell are demonstrated in Section 3. LEE values and distribution of the Poynting vectors' magnitude for six different DUV-LED structures are calculated and analyzed in Section 4. Those different structures are classified by whether the inclined sidewall is adopted, whether the optimized metasurface is applied, and whether the roughed  $n\text{-AlGaN}$  exists. Additionally, the  $p\text{-GaN}$ 's existence and what metallic layers are adopted between Ni/Au and Ni/Al become variables in this study. LEEs and power distributions of these structures are calculated for both TE and TM modes, respectively.

## 2. Modeling and Calculation Process

A unit cell structure is constructed to optimize and extract the metasurface's maximum transmittance on the  $n$ -type cladding epitaxial layer.  $n\text{-Al}_{0.65}\text{Ga}_{0.35}\text{N}$  Cylinder is selected as the resonator's shape triggering Mie resonance by assuming such resonators can be formed by etching  $n\text{-Al}_{0.65}\text{Ga}_{0.35}\text{N}$  flat epitaxial layer. The transparent view of the constructed unit cell is shown in Fig. 1(a). Fig. 1(b) and (c) show cross-sectional views of a YZ-plane cutting the middle of the  $x$ -axis and an XY-plane cutting the middle of the cylinder's height, respectively. The constant horizontal wavenumber approach is utilized to efficiently analyze the constructed unit cell [17]–[19]. The unit cell's each plane at the end of  $+x$ ,  $-x$ ,  $+y$ , and  $-y$  directions adopt periodic boundaries.  $+z$  and  $-z$  boundaries are set up with the convolutional perfectly matched layer (CPML) for efficient optical power absorption. The height of the unit cell  $h_u$  is decided and fixed as  $2.0 \mu\text{m}$  for the entire study. The Al compositional ratio  $x$  of  $\text{Al}_x\text{Ga}_{1-x}\text{N}$  is selected as the 0.65 to maintain transparency for the wavelength  $\lambda = 280$  nm. The distances between the  $n\text{-Al}_{0.65}\text{Ga}_{0.35}\text{N}$ /air interface and vertical boundaries maintain over 450 nm to remove the error stemming from evanescent waves. Here, the unit cell adopts the square lattice with the lattice constant  $a = 110$  nm. The resonant magnetic dipole response occurs when the wavelength inside a circular particle is comparable to the particle's diameter,  $\lambda/n_{\text{mat}} = D$  [15]. The  $D$  is about 110 nm when  $\lambda = 280$  nm, and the refractive index of  $n\text{-Al}_{0.65}\text{Ga}_{0.35}\text{N}$   $n_{\text{mat}} = 2.51$ . However, in our case, obtaining high transmittance is the goal, so the minimized backscattering at the top-side of the interface is desirable. Usually, these conditions can be satisfied with the resonator having a smaller diameter than  $D$  for a fixed  $\lambda$ . Therefore, we set up  $a = 110$  nm and optimize the size of the radius  $r$  and height of cylindrical  $\text{Al}_{0.65}\text{Ga}_{0.35}\text{N}$  resonator  $h$ . The unit cell is discretized by cubic Yee cells with 5 nm identical length's sides,  $dx = dy = dz = 5$  nm. The thickness of the  $\text{Al}_{0.65}\text{Ga}_{0.35}\text{N}$  epitaxial layer and unit time-step  $dt$  are fixed as  $1.455 \mu\text{m}$  and  $8.67 \times 10^{-18}$  s, respectively. For the transmittance calculation, a plane wave propagates starting from near the top-side CPML boundary, and a plane sensor is located

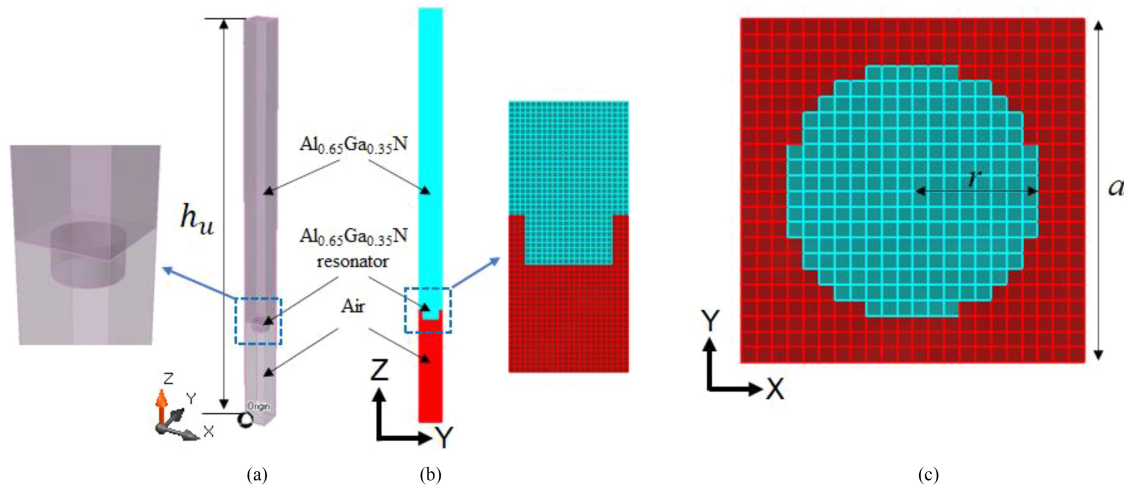


Fig. 1. (a) A transparent view of a unit cell adopting cylinder resonator on  $\text{Al}_{0.65}\text{Ga}_{0.35}\text{N}$ . (b) A cross-sectional view which is cutting the middle of the  $x$ -axis of the unit cell. (c) A cross-sectional view which is cutting the middle of the height of the cylinder resonator attached to  $\text{Al}_{0.65}\text{Ga}_{0.35}\text{N}$ . Grids represented in (b) and (c) mean boundaries between Yee cells.

beneath the XY-plane of the plane wave's starting position. The plane wave adopts the modulated Gaussian waveform. Running Fourier transform converts the time-based field data on the plane sensor to the frequency-based one. After the final time-marching steps, the plane sensor calculates time-averaged Poynting vectors, which are utilized to calculate transmittance. Additionally, the cross-sectional planes of Fig. 1(b) and (c) collect all field components' intensities for analysis. A unit cell is calculated twice with and without scatterers to calculate transmittance based on the Poynting theorem. The  $\text{Al}_{0.65}\text{Ga}_{0.35}\text{N}$  is fixed as the background material for all calculations based on the unit cell.

We investigate the optimized metasurface's influence on the LEE of DUV-LEDs after the unit cell's analysis. To compare with different flip-chip structures without AlGaIn metasurface, we construct 3D LED structures as shown in the transparent views of Fig. 2. Fig. 3 shows the cross-sectional views of each considered LED structure in Fig. 2(a)–(f). A total of six different flip-chip structures of (I, F), (I, R), (I, M), (S, F), (S, R), and (S, M) are considered in this study. Here, I, S, F, R, and M symbols mean infinite lateral chip area, the inclined sidewall, flat  $n\text{-Al}_{0.65}\text{Ga}_{0.35}\text{N}$  interface, roughed  $n\text{-Al}_{0.65}\text{Ga}_{0.35}\text{N}$  interface, and the optimized metasurface, respectively. Unit cells with  $dx = dy = 11$  nm and  $dz = 2$  nm discretize the DUV-LED's structures in the FDTD domains. Total  $x$ ,  $y$ , and  $z$  lengths of the FDTD domains are fixed as 2.75, 2.75, and 2  $\mu\text{m}$ , respectively. Fig. 2(a) structure is regarded as the reference in this study, and  $n\text{-Al}_{0.65}\text{Ga}_{0.35}\text{N}$  is located on  $z = 500$  nm with 455 nm thickness. The 455 nm  $n\text{-Al}_{0.65}\text{Ga}_{0.35}\text{N}$  may not be a realistic thickness, but it is enough to extract valid LEE tendency for the target wavelength. 60 nm  $\text{Al}_{0.5}\text{Ga}_{0.5}\text{N}$ , 100 nm  $\text{Al}_{0.75}\text{Ga}_{0.25}\text{N}$  electron blocking layer (EBL), 200 nm  $p\text{-Al}_{0.65}\text{Ga}_{0.35}\text{N}$ ,  $p\text{-GaN}$  (or additional  $p\text{-Al}_{0.65}\text{Ga}_{0.35}\text{N}$ ), and metallic layers are stacked up on  $n\text{-Al}_{0.65}\text{Ga}_{0.35}\text{N}$  in order. An  $\text{Al}_{0.5}\text{Ga}_{0.5}\text{N}$  layer simplifies the multiple quantum well (MQW) in this study. One of both  $\text{Ni}(40$  nm)/ $\text{Au}(100$  nm) and  $\text{Ni}(2$  nm)/ $\text{Al}(150$  nm) is inserted as the metallic layers. The Lorentz-Drude model is adopted for the description of Ni, Au, and Al [20], [21]. Fig. 2(b) and (c) are the structures adding roughed  $n\text{-Al}_{0.65}\text{Ga}_{0.35}\text{N}$  right circular cones and the metasurface, respectively, on the bottom-side  $n\text{-Al}_{0.65}\text{Ga}_{0.35}\text{N}$  flat epitaxial layer of the reference structure. The adopted cones have the height  $h = 200$  nm, radius  $r = 99$  nm, and opening angle  $52.7^\circ$ . The cones are uniformly distributed with square lattice and a lattice constant of 209 nm. Fig. 2(d), (e), and (f) are the cases when the structures of Fig. 2(a), (b), and (c) adopts the inclined sidewalls, respectively. About 45 degrees of identical inclined walls are applied to each structure of Fig. 2(d)–(f), and the inclination extends from the Ni's bottom plane to 200 nm

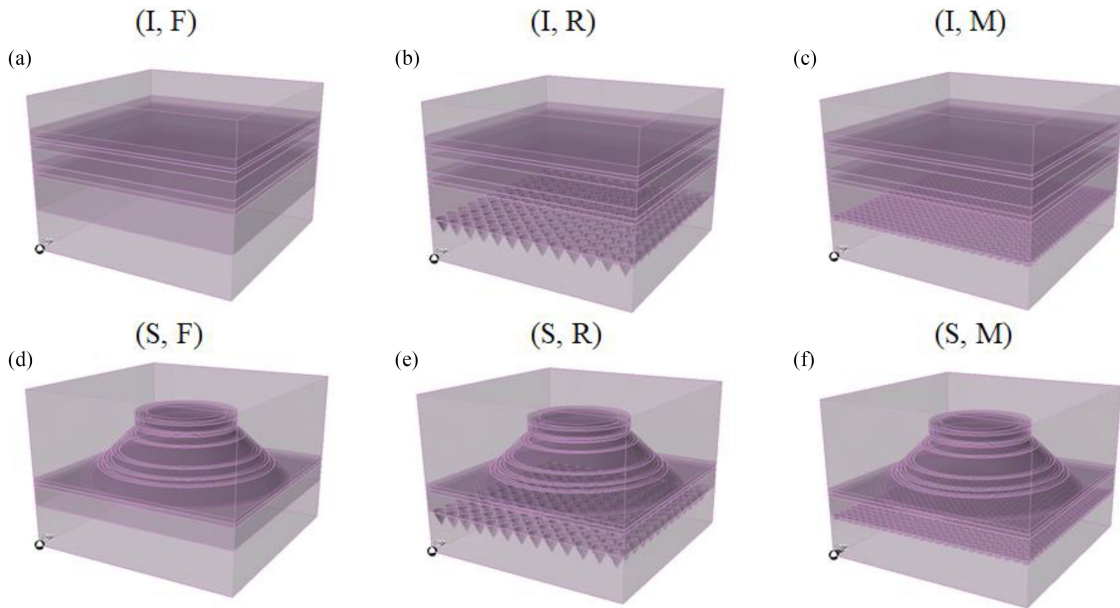


Fig. 2. In this figure, I, S, F, R, and M mean the assumption of infinite lateral area, inclined sidewall, flat n-AlGaN, roughed n-AlGaN, and AlGaN metasurface, respectively. Therefore, these figures show LED structures (a) adopting the infinite lateral area with flat n-AlGaN, (b) the infinite lateral area with roughed n-AlGaN, (c) the infinite lateral area with the optimized AlGaN metasurface, (d) the inclined sidewall with flat n-AlGaN, (e) the inclined sidewall with roughed n-AlGaN, and (f) the inclined sidewall with the AlGaN metasurface, respectively. For the description of the roughed n-AlGaN, we adopt the uniformly deployed cones with height  $h = 200$  nm and radius  $r = 99$  nm.

TABLE 1  
The Material Parameters Used for the Entire Analysis of This Study

| Material   | $\epsilon_{r,real}$ | $\epsilon_{r,imag}$ | Ref. |
|--|---------------------|---------------------|------|
| Ni   | Lorentz-Drude model |                     | [20] |
| Au   | Lorentz-Drude model |                     | [20] |
| Al   | Lorentz-Drude model |                     | [20] |
| p-GaN  | 8.27                | 2.20                | [22] |
| MQW: Al <sub>0.5</sub> Ga <sub>0.5</sub> N       | 7.90                | 0.0124              | [7]  |
| p- and n-Al <sub>0.65</sub> Ga <sub>0.35</sub> N | 6.30                | 0                   | [7]  |
| EBL: Al <sub>0.75</sub> Ga <sub>0.25</sub> N     | 5.71                | 0                   | [7]  |
| SiO <sub>2</sub>                                 | 2.23                | 0                   | [23] |

etched n-Al<sub>0.65</sub>Ga<sub>0.35</sub>N. The inclined walls are coated with SiO<sub>2</sub>/Al (about 35/35 nm), as shown in Fig. 3(d)–(f). Ni, Au, and Al's diameter are maintained as 1.1  $\mu\text{m}$  for structures adopting inclined sidewall. The unit time-step  $dt$  is set up as  $1.29 \times 10^{-18}$  s by considering Al's small refractive index  $n > 0.2$  at  $\lambda = 270\sim 300$  nm. All material parameters used in this study are listed in Table 1 with references.  $-z$  and  $+z$  boundaries are set up with CPML, which is the same as the unit cell case. The perfect electric conductor (PEC) is positioned at the  $-x$ ,  $+x$ ,  $-y$ , and  $+y$  boundaries to truncate the infinite lateral area or periodicity. Each simulation process ends after  $8 \times 10^5$  iterations of the time-marching steps. An electric dipole source is set up at the center of MQW for the generation of Gaussian waveform with a selected polarity, TE or TM mode. Here, TE and TM modes are defined as the electric dipole oscillating parallel to the n-AlGaN flat surface and the electric dipole oscillating normal to the n-AlGaN flat surface, respectively. A monitoring box encapsulates the dipole source to calculate the total emitted power generated by the dipole and calculate the absorbed power inside the box. Additionally, a plane sensor is installed near the bottom-side CPML boundary to calculate the escaped light power from the LED to air.

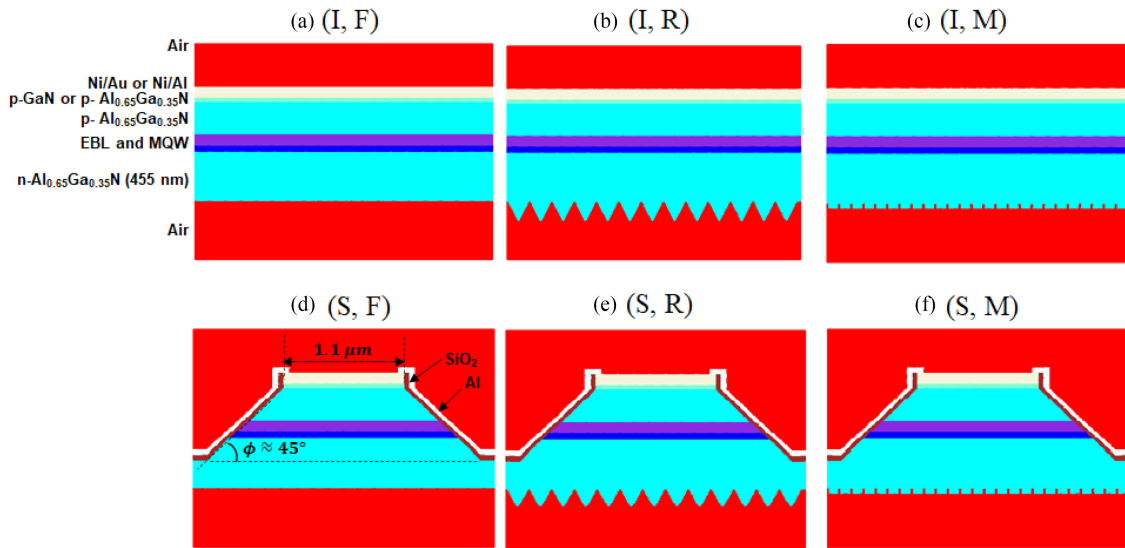


Fig. 3. (a)–(f): The cross-sectional views at the cutlines of the middle of the  $y$ -axis of Fig. 2(a)–(f), respectively.

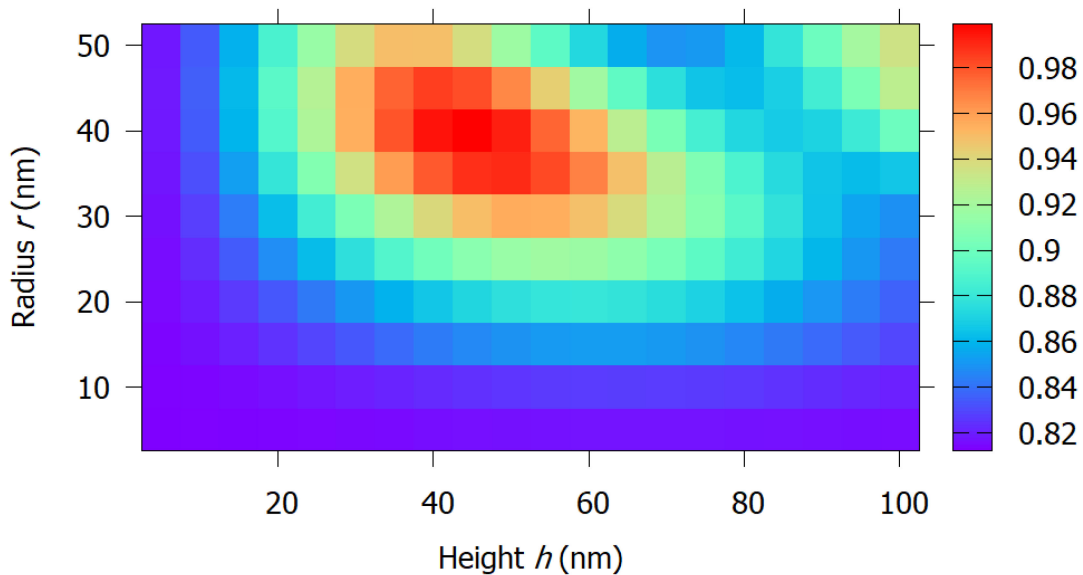


Fig. 4. Transmittance map constructed as functions of the radius  $r$  and height  $h$  of cylinder resonator of Fig. 1(a) when a normal incidence plane wave is injected.

### 3. Optimization and Analysis of a Unit Cell

For optimizing the cylinder resonator in Fig. 1, we construct a transmittance map at  $\lambda = 280$  nm as functions of the radius  $r$  and height  $h$  of the cylinder when a normal incidence plane wave propagates starting from near the  $+z$  boundary. Fig. 4 shows the constructed transmittance map as a result. The high transmittance region focuses on the intersection between  $h = 40\sim 50$  and  $r = 35\sim 45$  nm. We select  $r = 40$  and  $h = 45$  nm to calculate the unit cell's incidence angle-dependent transmittance. Then, transmittances for TE and TM modes of the flat n-AlGaIn and the metasurface were calculated as functions of the frequency and wavenumber  $k$ , as shown in Fig. 5. Here,  $k$  means the horizontal wavenumber related to the periodic boundaries of  $\pm x$  and  $\pm y$  axis. The relation

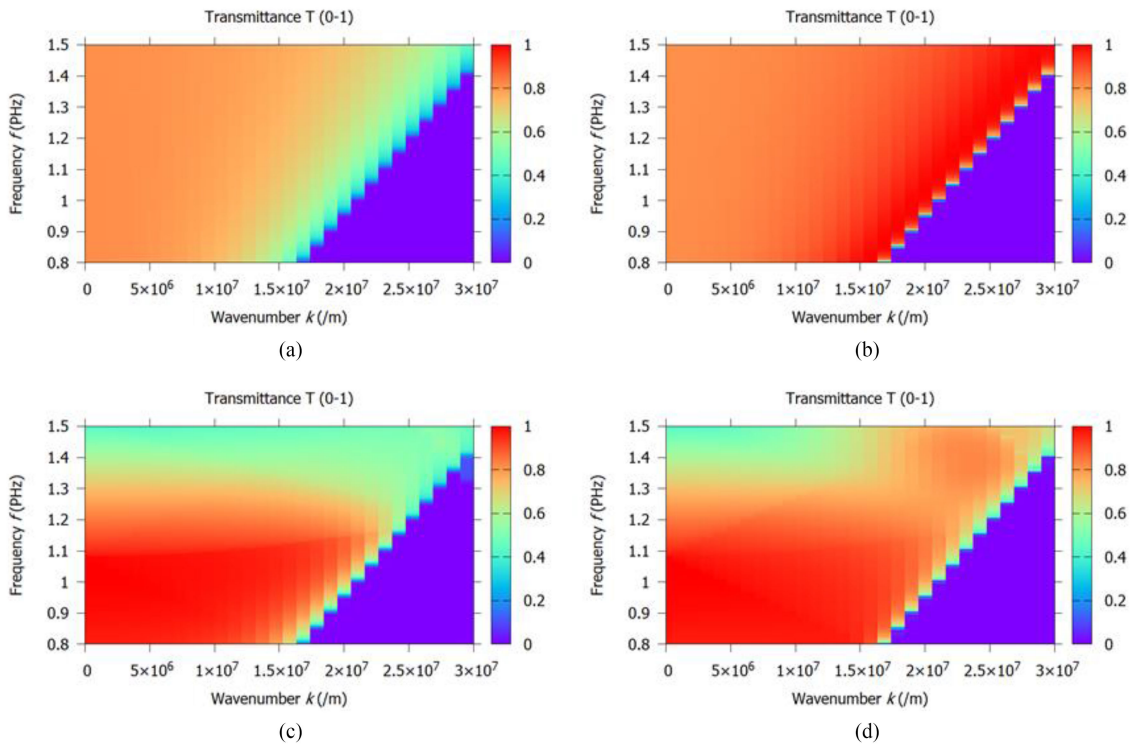


Fig. 5. (a) and (b) show transmittance maps with flat  $\text{Al}_{0.65}\text{Ga}_{0.35}\text{N}$  for TE and TM modes, respectively, as functions of the horizontal wavenumber  $k$  and frequency  $f$ . (c) and (d) show transmittance maps with the optimized AlGaIn metasurface for TE and TM modes, respectively, as functions of  $k$  and  $f$ .

between the  $k$  and incidence angle  $\theta$  is as the (1) following.

$$k = k_0 \sin\theta \quad (1)$$

where  $k_0 = \omega/c$  is the wavenumber with angular frequency  $\omega$  and the speed of light  $c$  in the material [17]. (1) implies that the identical  $\theta$  at different frequencies is satisfied at the different  $k$  values. Here,  $k$  equals to  $\sqrt{k_x^2 + k_y^2}$  where  $k_x$  and  $k_y$  represent the horizontal wavenumbers at the boundaries of  $\pm x$  and  $\pm y$ , respectively. For the gradual increase of  $\theta$ , the only  $k_y$  was controlled as a variable during the unit cell's analysis, and  $k_x$  is fixed as zero. Fig. 5(a)–(d) represents the transmittance maps for flat  $n\text{-Al}_{0.65}\text{Ga}_{0.35}\text{N}/\text{air}$  interface with TE mode  $n\text{-Al}_{0.65}\text{Ga}_{0.35}\text{N}/\text{air}$  with TM mode, metasurface/air with TE mode, and metasurface/air with TM mode, respectively. The stair-like area colored by the violet in the maps means perfect reflection due to TIR. The critical angle in Fig. 5 is about  $23.48^\circ$ . The increase of TM mode light's transmittance as a function of incidence angle in Fig. 5(b) originates from Brewster's angle,  $21.72^\circ$ . After Brewster's angle, the transmittance abruptly decreases toward zero before the critical angle point. The broadbands of Fig. 5(c) and (d) between 0.8 PHz ( $\approx 375$  nm) and 1.1 PHz ( $\approx 273$  nm) show generally higher transmittance than Fig. 5(a) and (b) before the critical angle, which implies the optimized metasurface can contribute to increasing the LEE at least than the flat interface, but TIR is a still limitation. It has been recently reported that to relax TIR is possible by evanescent wave engineering [24]. We expect high transmittance metasurface, which can simultaneously circumvent TIR, may be possible in the near future, but such structure is beyond this study's topic. Fig. 6 shows the transmittance at both  $\lambda = 280$  nm and  $\lambda = 300$  nm as a function of  $\theta$ . Fig. 6 additionally includes the analytical results for the flat AlGaIn interfaces. The analytical transmittances are calculated by solving the Fresnel equations, and the  $k$  is converted into  $\theta$ . The results of Fig. 6 represent the excellent accuracy of the numerical results

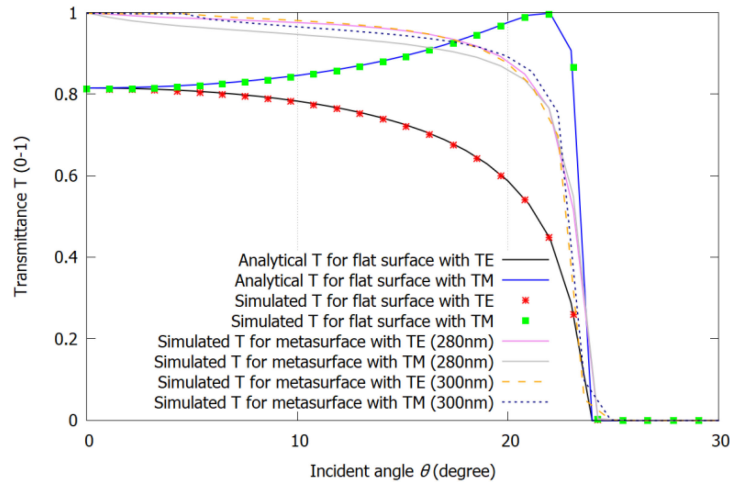


Fig. 6. Analytical and numerical results for each component of Fig. 5(a)–(d) at both  $\lambda = 280$  nm and  $\lambda = 300$  nm.

based on the unit cell. Also, it clearly shows the overall increase of transmittance after adopting the AlGaIn metasurface.

After analyzing transmittance, we observe the electromagnetic field distributions near the resonator when the normally incident plane wave is injected. The plots in Fig. 7(a)–(c) show  $\sqrt{|E_x|^2 + |E_y|^2}$ ,  $\sqrt{|E_x|^2 + |E_z|^2}$ , and  $\sqrt{|E_y|^2 + |E_z|^2}$  at the XY-plane cutting the middle of the cylinder height, the XZ-plane cutting the middle of the y-axis of the unit cell, and the YZ-plane cutting the middle of the x-axis of the unit cell, respectively. Similarly, Fig. 7(d)–(f) present  $\sqrt{|H_x|^2 + |H_y|^2}$  at the XY-plane cutting the middle of cylinder height,  $\sqrt{|H_x|^2 + |H_z|^2}$  at the XZ-plane cutting the middle of the y-axis of the unit cell, and  $\sqrt{|H_y|^2 + |H_z|^2}$  at the YZ-plane cutting the middle of the x-axis of the unit cell, respectively.  $E_i = x, y, z$  and  $H_i = x, y, z$  mean the electric field components and the magnetic field components, respectively, in the frequency domain's cartesian coordinate. Fig. 7 simultaneously offers the normalized vector distributions, which show the field components' direction at each figure. Those vectors have consisted of the real part of the electric field components or the magnetic field components. The cylinder resonator exists on  $z = 500$  nm with  $h = 45$  nm. Magnetic and electric dipoles crossing each other are observed by the vector plots of Fig. 7(c) and (e), respectively, right below the resonator. An additional magnetic dipole exists right above the cylinder resonator, as shown in Fig. 7(c). The crossed electric and magnetic dipoles consist of Huygens' sources [25], [26]. The resonances near the resonator remove the backscattering by the destructive interference and make it possible to attain the nearly perfect transmittance at normal incidence.

The smaller dimension of the optimized AlGaIn resonator requires more massive computational resources when the LEE is calculated with the chip area over  $2.75 \times 2.75 \mu\text{m}^2$ . We slightly broaden the unit cell's discretization length as  $dx = dy = 11$  nm to reduce the required computational resource. More coarse discretization may produce lesser accuracy of the geometrical description. However, we confirm that the increased geometrical error rate does not trigger a considerable characteristic change of the cylinder resonator, as shown in Fig. 8.

#### 4. Comparison of LEEs of Flip-Chip DUV-LEDs

In this section, we estimate and discuss the LEEs of DUV-LEDs for the structures in Fig. 2. Fig. 9(a)–(d) show the calculated LEEs of Fig. 2(a)–(c)'s structures for TE and TM modes when



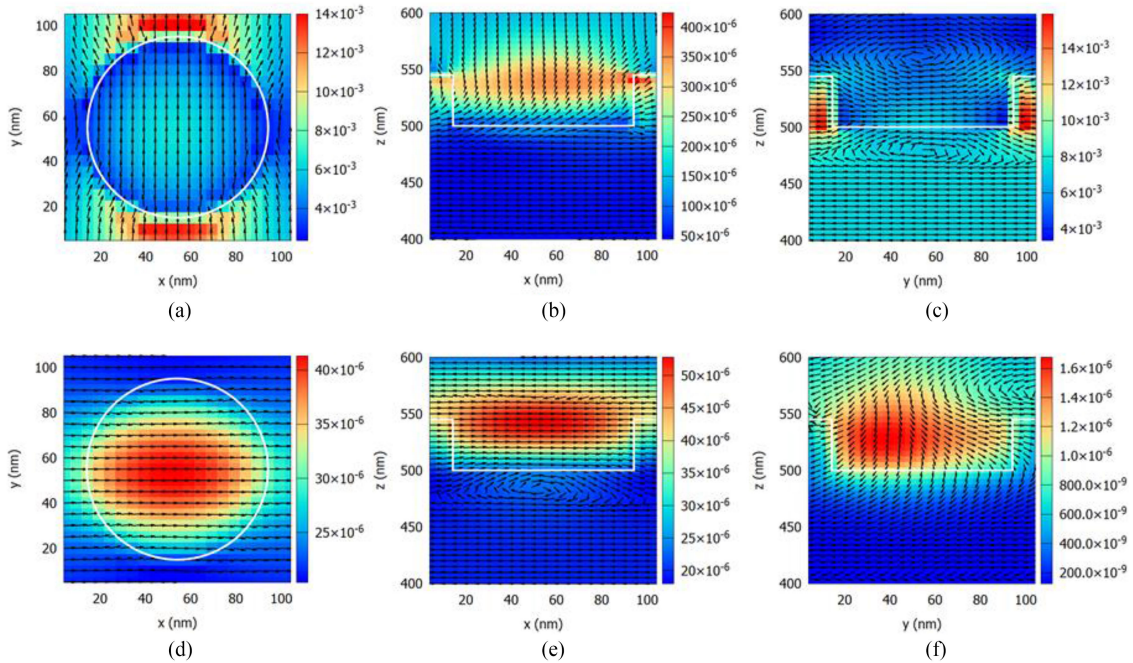


Fig. 7. Direction and magnitude of fields at  $\lambda = 280$  nm: (a) Distribution of  $\sqrt{|\mathbf{E}_x|^2 + |\mathbf{E}_y|^2}$  at the XY-plane cutting the middle of the height of the cylinder, (b) Distribution of  $\sqrt{|\mathbf{E}_x|^2 + |\mathbf{E}_z|^2}$  at the XZ-plane cutting the middle of the unit cell's  $y$ -axis near the cylinder resonator, (c) Distribution of  $\sqrt{|\mathbf{E}_y|^2 + |\mathbf{E}_z|^2}$  at the YZ-plane cutting the middle of the unit cell's  $x$ -axis near the cylinder resonator, (d) Distribution of  $\sqrt{|\mathbf{H}_x|^2 + |\mathbf{H}_y|^2}$  at the XY-plane cutting the middle of the height of the cylinder, (e) Distribution of  $\sqrt{|\mathbf{H}_x|^2 + |\mathbf{H}_z|^2}$  at the XZ-plane cutting the middle of the unit cell's  $y$ -axis near the cylinder resonator, (f) Distribution of  $\sqrt{|\mathbf{H}_y|^2 + |\mathbf{H}_z|^2}$  at the YZ-plane cutting the middle of the unit cell's  $x$ -axis near the cylinder resonator. (a)–(f) additionally show the normalized vector showing the direction of each figure's field components. Solid lines mean the interfaces between n-AlGaIn and air.

Ni/Au metal layers are adopted as a function of p-GaN or p-Al<sub>0.65</sub>Ga<sub>0.35</sub>N thicknesses. Periodically varying LEEs are due to the interference of downward emitted light and upward reflected light. In Fig. 9, the metasurface seems uniformly elevates LEE with about a fixed ratio regardless of the p-type cladding layer's thickness compared with the flat n-Al<sub>0.65</sub>Ga<sub>0.35</sub>N interface. These phenomena occur due to the two factors. First, highly absorbed photon energy in the Ni/Au and p-GaN even for the short traveling time of photon at the top-side of DUV-LED structures. Second, both flat and metasurface interfaces maintain TIR over the critical angle, 23.5°. Since the roughed interface breaks the TIR and offers various incidence angles for light extraction, the LEE for TM mode increases more than two times better than the optimized metasurface, as shown in Fig. 9(c) and (d). Extracted results in Fig. 9 imply that it will be essential to force the incidence angle of light at the bottom-side interface within the critical angle to maximize the functionality of the optimized metasurface as a light extractor. Without the engineering to offer the appropriate incidence angles, the maximum LEEs for TE and TM modes will be below about 6% and 5%, respectively, with Ni/Au structures.

It has been reported that p-AlGaIn/thin Ni/Al can efficiently suppress light absorption in DUV-LEDs [11]. We calculated its influence on LEE for the structures Fig. 2(a)–(f) as shown in Fig. 10 and compared it with Ni/Au cases. Within the assumption of infinite lateral chip area, giving a roughness on n-Al<sub>0.65</sub>Ga<sub>0.35</sub>N with p-Al<sub>0.65</sub>Ga<sub>0.35</sub>N/Ni/Al (100/2/15 nm) records the 12.9% and 11.8% LEEs

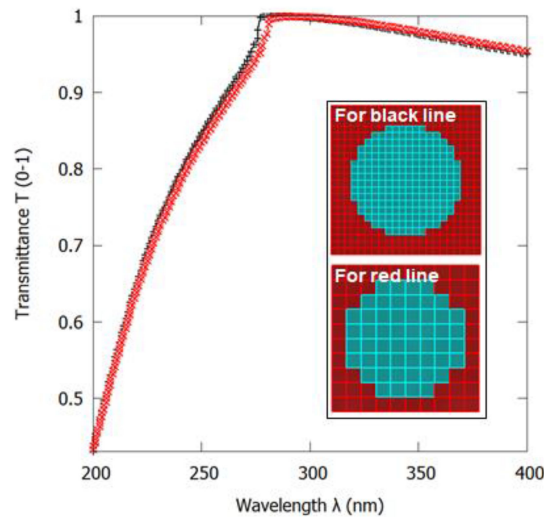


Fig. 8. Transmittances as a function of the wavelength when  $dx = dy = 5$  or  $11$  nm. The  $5$  nm discretization was used for the unit cell-based calculations and optimization. The  $11$  nm discretization was used for the LEE calculations.

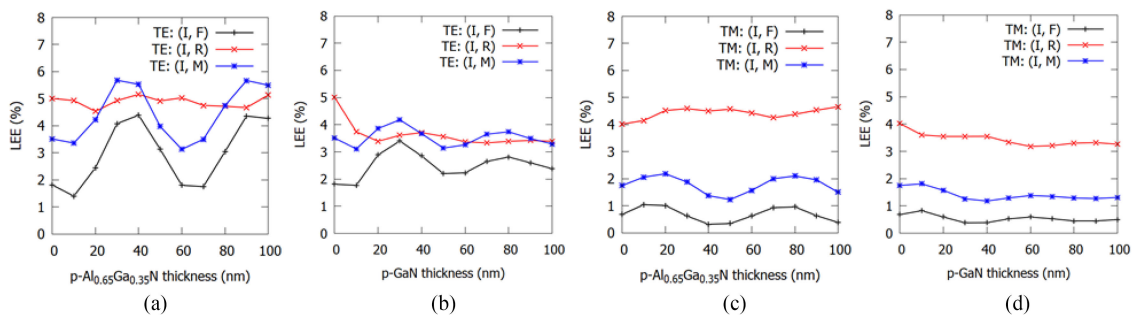


Fig. 9. LEEs with the structures adopting Ni( $40$  nm)/Au( $100$  nm) metal layers as a function of the p-GaN or p-Al $_{0.65}$ Ga $_{0.35}$ N thickness: LEE for TE mode of Fig. 2(a)–(c) structures as a function of (a) p-Al $_{0.65}$ Ga $_{0.35}$ N or (b) p-GaN thickness, respectively. LEE for TM mode of Fig. 2(a)–(c) structures as a function of (c) p-Al $_{0.65}$ Ga $_{0.35}$ N or (d) p-GaN thickness, respectively.

for TE and TM modes, respectively, as shown in Fig. 10(a). Those LEEs are over twice than the cases of Ni/Au/p-Al $_{0.65}$ Ga $_{0.35}$ N. The LEEs with AlGaN metasurface are  $9.09\%$  and  $5\%$  for TE and TM modes, respectively, within the assumption of the infinite lateral length. Extracted results show that breaking TIR is a critical point to increase LEE, which is coherent with the previous reports. Fig. 10(a) also shows that highly reflective Ni/Al metal layers become meaningful only when the thick p-GaN does not exist due to its large absorption coefficient. When p-GaN is employed, the alteration of LEE becomes negligible even after adopting Ni/Al.

Al/SiO $_2$  inclined sidewall offers the appropriate feature to focus the incidence angle of light within the bottom-side interface's critical angle. Also, laterally propagating light is forced to tilt its propagation direction with a small loss. Its structural angle-dependent effect was systematically studied recently [27]. We fixed the sidewall angle to about  $45^\circ$  and investigated its effect on LEE for the structures of Fig. 2(d)–(f). Electric dipole source polarized parallel to the flat n-Al $_{0.65}$ Ga $_{0.35}$ N/air interface creates TE mode wave against the bottom-side interface. However, against the sidewall, both TE and TM modes are generated. The electric dipole source vertically polarized to the flat n-Al $_{0.65}$ Ga $_{0.35}$ N/air generates TM mode against the bottom-side interface and TE mode against the sidewall direction. Fig. 10(b) shows that tilting the direction of laterally propagating light to the bottom direction should significantly increase the LEE. In this case, offering additional roughness at

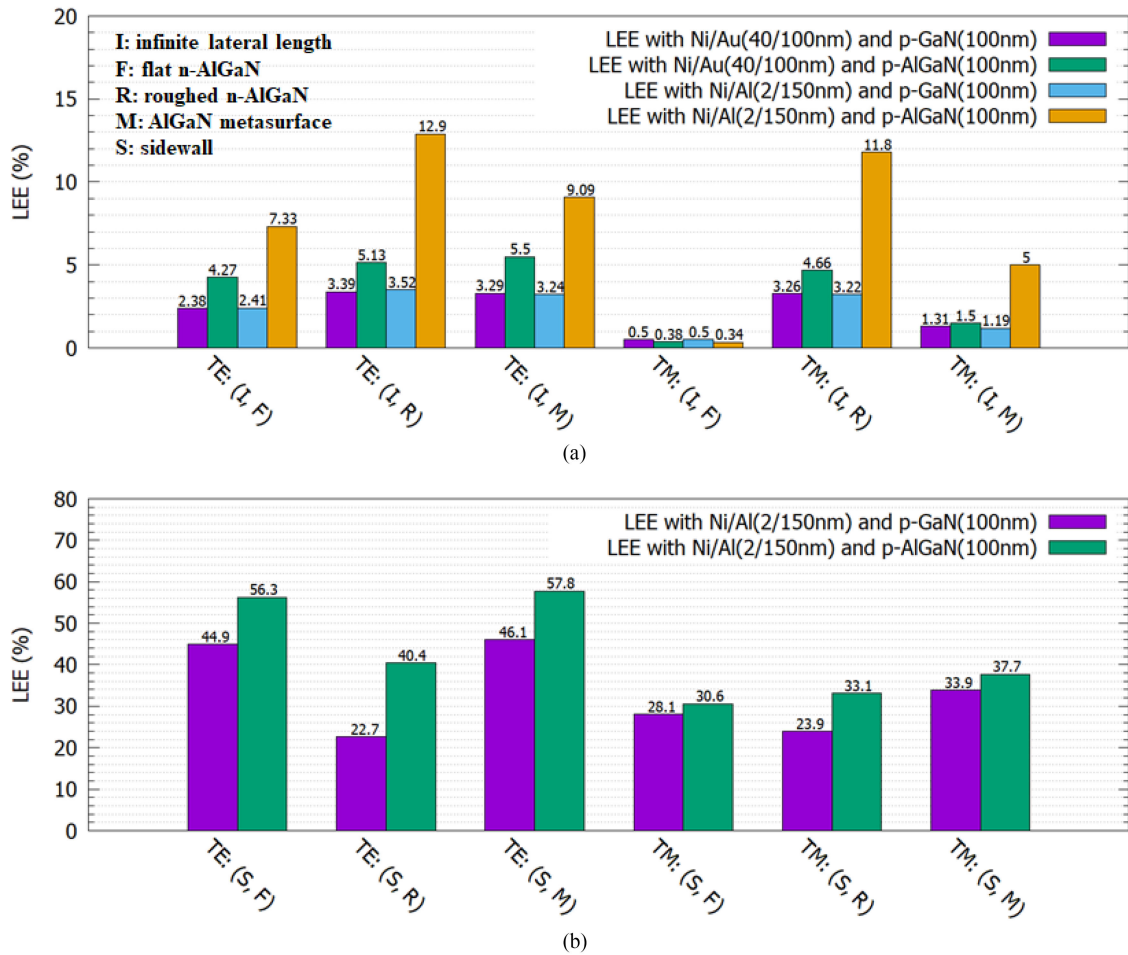


Fig. 10. LEEs for the structures of Fig. 2(a)–(f) with fixed 100 nm p-GaN or p-Al<sub>0.65</sub>Ga<sub>0.35</sub>N thickness. Adopting the inclined sidewall, Ni/Al, Ni/Au, p-GaN, or p-Al<sub>0.65</sub>Ga<sub>0.35</sub>N becomes variables for the analysis. (a) and (b) show the results of LEEs without and with inclined sidewall, respectively. The caption on each bar represents the LEE value for the given structure.

the AlGaN/air interface may trigger an antagonistic effect, as shown by the Fig. 10(b). 56.3% LEE for p-AlGaN/Ni/Al TE: (S, F) is lowered to 40.4% with the additional roughness. The comparison between TM: (S, F) and TM: (S, R) shows a 2.5% increase after adopting the typical roughness, but its increment is too small compared with the loss in TE mode light. When the metasurface is adopted, always a positive increase of LEE is observed in Fig. 10(b) regardless of the species of p-type cladding layers and polarizability. The positive effect of the combination of inclined sidewall and metasurface increases 56.3% and 30.6% LEEs for TE: (S, F) to 57.8% and 37.7%, respectively.

As the next step, we analyze the averaged Poynting vector distributions to observe where the optical power is mainly localized. Figs. 11 and 12 show the normalized magnitude of Poynting vector  $P_m = \sqrt{P_x^2 + P_y^2 + P_z^2}$  at the XZ-plane cutting the middle of the y-axis for TE and TM modes, respectively.  $P_x$ ,  $P_y$ , and  $P_z$  mean the time-averaged Poynting vectors of x-, y- and z-directions at a point, respectively. The colors of all figures in Fig. 11 and 12 represent the legend's values at both Fig. 11(f) and Fig. 12(f)'s right-sides. 100 nm p-Al<sub>0.65</sub>Ga<sub>0.35</sub>N and Ni/Al layers are fixed as the commonly shared structural parameters for both Fig. 11 and 12. Fig. 11(a)–(c) and Fig. 12(a)–(c) show that both TE and TM modes adopting large lateral area will have laterally localized optical power. Clearer contrast of power focused laterally in Fig. 12(a)–(c) than Fig. 11(a)–(c) means that

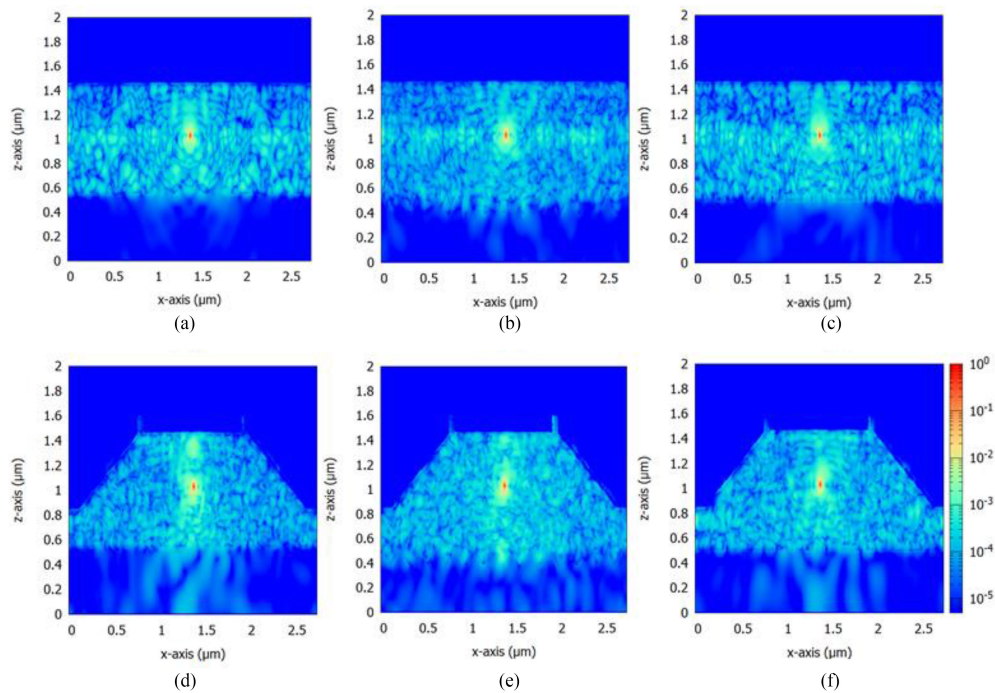


Fig. 11. Distribution of the normalized magnitude of Poynting vector at XZ-plane cutting the middle of the y-axis for TE mode: the structures of (a)–(f) adopt (I, F), (I, R), (I, M), (S, F), (S, R), and (S, M), respectively. All structures also adopt Ni/Al(2/150 nm) and 100 nm p-Al<sub>0.65</sub>Ga<sub>0.35</sub>N.

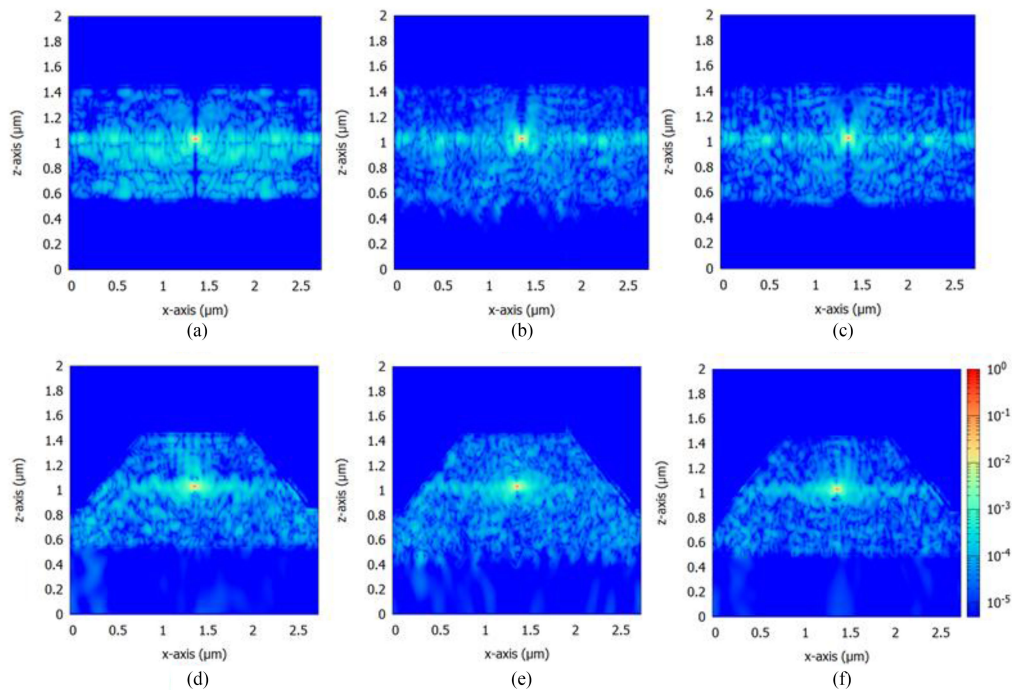


Fig. 12. Distribution of the normalized magnitude of Poynting vector at XZ-plane cutting the middle of the y-axis for TM mode: the structures of (a)–(f) adopt (I, F), (I, R), (I, M), (S, F), (S, R), and (S, M), respectively. The all structures also adopt Ni/Al(2/150 nm) and 100 nm p-AlGa<sub>N</sub>.

the laterally localized power for TM modes is quite severe. The ratio of laterally localized optical power for TE mode is significantly lowered after employing the inclined sidewall, as shown by Fig. 11(d)–(f). However, in the case of TM mode with the sidewall, Fig. 12(d)–(f), the laterally localized optical power is still strong, which is related to the lower LEE than the counterparts of TE mode. This laterally localized power comes from the active region's guided wave due to the higher refractive index  $n$  of MQW than both EBL and n-AlGaIn. By introducing some scattering structure into the active region, which can scatter the laterally guided wave, this problem may be solved, but the fabrication process and leakage current will be more challenging [7]. Additionally, in Fig. 11 and Fig. 12, a large portion of optical power is circulating inside entire LED structures. The Ni/Al layers will rapidly absorb such light, and it is why the power contrast between the active region and other layers is clear. To suppress the absorption by Ni/Al, utilization of the photonic crystal nearby the metal layers may be useful [28]. Since even the 2 nm Ni can significantly lower the reflectance at Ni/Al layers, an effective strategy to block the propagating light toward the top-side with low loss is a key to increasing LEE.

## 5. Conclusion

In this study, we compared LEEs among six different flip-chip structures and discussed how to increase further LEEs based on the extracted results. AlGaIn metasurface highly increases transmittance before the critical angle, but TIR has remained. Therefore, utilizing AlGaIn metasurface alone is inefficient, but a combination with the inclined sidewall can trigger a synergetic effect. Since spatial time-averaged Poynting vector shows that the localized optical power for TE and TM modes still strong even after adopting both sidewall and metasurface, additional treatments are necessary to scatter laterally propagating light in the active region and to suppress the absorption by Ni for further LEE increment.

## Acknowledgment

RIKEN's HOKUSAI supercomputer system was utilized to calculate all contents in this study. Also, the authors appreciate the financial and indirect supports by the SPDR program provided by RIKEN.

## References

- [1] H. Hirayama, N. Maeda, S. Fujikawa, S. Toyoda, and N. Kamata, "Recent progress and future prospects of AlGaIn diodes," *Jpn. J. Appl. Phys.*, vol. 53, no. 10, 2014, Art. no. 100209.
- [2] M. Kneissl, T. Y. Seong, J. Han, and H. Amano, "The emergence and prospects of deep-ultraviolet light-emitting diode technologies," *Nat. Photon.*, vol. 13, no. 4, pp. 233–244, 2019.
- [3] S. E. Beck *et al.*, "Evaluating UV-C LED disinfection performance and investigating potential dual-wavelength synergy," *Water Res.*, vol. 109, pp. 207–216, Feb. 2017.
- [4] T. Takano, T. Mino, J. Sakai, N. Noguchi, K. Tsubaki, and H. Hirayama, "Deep-ultraviolet light-emitting diodes with external quantum efficiency higher than 20% at 275 nm achieved by improving light-extraction efficiency," *Appl. Phys. Exp.*, vol. 10, no. 3, pp. 6–10, 2017.
- [5] J. Li and G.-Q. Zhang, *Light-Emitting Diodes: Materials, Processes, Devices Applications*. Cham, Switzerland: Springer, 2019, pp. 337–396.
- [6] J. Yun, J. I. Shim, and H. Hirayama, "Analysis of efficiency droop in 280-nm AlGaIn multiple-quantum-well light-emitting diodes based on carrier rate equation," *Appl. Phys. Exp.*, vol. 8, no. 2, 2015, Art. no. 022104.
- [7] J. Yun and H. Hirayama, "Investigation of the light-extraction efficiency in 280 nm algan-based light-emitting diodes having a highly transparent p-AlGaIn layer," *J. Appl. Phys.*, vol. 121, no. 1, 2017, doi: [10.1063/1.4973493](https://doi.org/10.1063/1.4973493).
- [8] C. Frankerl *et al.*, "Strongly localized carriers in Al-rich AlGaIn/AlN single quantum wells grown on sapphire substrates," *J. Appl. Phys.*, vol. 127, no. 9, 2020, doi: [10.1063/1.5144152](https://doi.org/10.1063/1.5144152).
- [9] J. Yun, D. P. Han, and H. Hirayama, "Random electric field induced by interface roughness in GaN/Al<sub>x</sub>Ga<sub>1-x</sub>N multiple quantum wells," *Appl. Phys. Exp.*, vol. 12, no. 12, 2019, doi: [10.7567/1882-0786/ab548a](https://doi.org/10.7567/1882-0786/ab548a).
- [10] M. Shatalov *et al.*, "High power AlGaIn ultraviolet light emitters," *Semicond. Sci. Technol.*, vol. 29, no. 8, 2014, doi: [10.1088/0268-1242/29/8/084007](https://doi.org/10.1088/0268-1242/29/8/084007).
- [11] N. Maeda, J. Yun, M. Jo, and H. Hirayama, "Enhancing the light-extraction efficiency of AlGaIn deep-ultraviolet light-emitting diodes using highly reflective ni/mg and rh as p-type electrodes," *Jpn. J. Appl. Phys.*, vol. 57, no. 4, pp. 2–6, 2018.

- [12] J. J. Wierer, A. A. Allerman, I. Montaño, and M. W. Moseley, "Influence of optical polarization on the improvement of light extraction efficiency from reflective scattering structures in AlGaIn ultraviolet light-emitting diodes," *Appl. Phys. Lett.*, vol. 105, no. 6, 2014, doi: [10.1063/1.4892974](https://doi.org/10.1063/1.4892974).
- [13] M. Jo, N. Maeda, and H. Hirayama, "Enhanced light extraction in 260 nm light-emitting diode with a highly transparent p-AlGaIn layer," *Appl. Phys. Exp.*, vol. 9, no. 1, pp. 5–8, 2016.
- [14] Y. Kivshar and A. Miroshnichenko, "Meta-Optics with mie resonances," *Opt. Photon. News*, vol. 28, no. 1, pp. 24, 2017, doi: [10.1364/opn.28.1.000024](https://doi.org/10.1364/opn.28.1.000024).
- [15] A. I. Kuznetsov, A. E. Miroshnichenko, M. L. Brongersma, Y. S. Kivshar, and B. Luk'yanchuk, "Optically resonant dielectric nanostructures," *Science*, vol. 354, 2016, Art. no. 6314.
- [16] U. Tisch, B. Meyler, O. Katz, E. Finkman, and J. Salzman, "Dependence of the refractive index of Al<sub>x</sub>Ga<sub>1-x</sub>N on temperature and composition at elevated temperatures," *J. Appl. Phys.*, vol. 89, no. 5, pp. 2676–2685, 2001.
- [17] K. ElMahgoub, F. Yang, and A. Elsherbeni, *Scattering Analysis of Periodic Structures Using Finite-Difference Time-Domain Method*. San Rafael, CA, USA: Morgan & Claypool, 2012, pp. 1–60.
- [18] A. Z. Elsherbeni and V. Demir, *The Finite-Difference Time-Domain Method for Electromagnetics with MATLAB Simulations*, 2nd ed. Edison, NJ, UK: SciTECH Publishing, 2016, pp. 413–446.
- [19] J. Yun, Y. Kashima, and H. Hirayama, "Reflectance of a reflective photonic crystal p-contact layer for improving the light-extraction efficiency of algan-based deep-ultraviolet light-emitting diodes," *AIP Adv.*, vol. 8, no. 12, 2018, doi: [10.1063/1.5062603](https://doi.org/10.1063/1.5062603).
- [20] A. D. Rakić, A. B. Djurišić, J. M. Elazar, and M. L. Majewski, "Optical properties of metallic films for vertical-cavity optoelectronic devices," *Appl. Opt.*, vol. 37, no. 22, 1998, Art. no. 5271.
- [21] A. A. Al-Jabr and M. A. Alsunaidi, "A general ADE-FDTD algorithm for the simulation of different dispersive materials," *Prog. Electromagn. Res. Symp.*, vol. 1, no. 12, pp. 268–271, 2009.
- [22] H. Y. Ryu, "Large enhancement of light extraction efficiency in algan-based nanorod ultraviolet light-emitting diode structures," *Nanoscale Res. Lett.*, vol. 9, no. 1, pp. 1–7, 2014.
- [23] I. H. Malitson, "Interspecimen comparison of the refractive index of fused silica," *J. Opt. Soc. Amer.*, vol. 55, no. 10, 1965, Art. no. 1205.
- [24] S. Jahani and Z. Jacob, "Breakthroughs in photonics 2014: Relaxed total internal reflection," *IEEE Photon. J.*, vol. 7, no. 3, Jun. 2015, Art. no. 0700505.
- [25] W. Liu and Y. S. Kivshar, "Generalized kerker effects in nanophotonics and meta-optics," *Opt. Exp.*, vol. 26, no. 10, pp. 274–284, 2017.
- [26] M. Decker *et al.*, "High-efficiency dielectric huygens' surfaces," *Adv. Opt. Materials*, vol. 3, no. 6, pp. 813–820, 2015.
- [27] Y. Zheng *et al.*, "Understanding omni-directional reflectors and nominating more dielectric materials for deep ultraviolet light-emitting diodes with inclined sidewalls," *J. Appl. Phys.*, vol. 128, no. 9, 2020, doi: [10.1063/5.0019650](https://doi.org/10.1063/5.0019650).
- [28] Y. Kashima *et al.*, "High external quantum efficiency (10%) algan-based deep-ultraviolet light-emitting diodes achieved by using highly reflective photonic crystal on p-AlGaIn contact layer," *Appl. Phys. Exp.*, vol. 11, no. 1, 2018, doi: [10.7567/APEX.11.012101](https://doi.org/10.7567/APEX.11.012101).